

## Enhanced terahertz radiation generated by intense laser interaction with a two-layer thin solid target

J. Y. Hua<sup>1,2</sup>, X. B. Zhang<sup>1,2,4</sup>, M. Chen<sup>1,2</sup>, S. M. Weng<sup>1,2</sup>, Y. P. Chen<sup>1,2</sup> and Z. M. Sheng<sup>1,2,3,\*</sup>

<sup>1</sup>Key Laboratory for Laser Plasmas (MoE), School of Physics and Astronomy, Shanghai Jiao Tong University, Shanghai 200240, China

<sup>2</sup>Collaborative Innovation Center of IFSA, Shanghai Jiao Tong University, Shanghai 200240, China

<sup>3</sup>Tsung-Dao Lee Institute, Shanghai Jiao Tong University, Shanghai 200240, China

<sup>4</sup>College of Physics and Electronic Engineering, Northwest Normal University, Lanzhou 730070, China

 (Received 19 December 2023; revised 3 July 2024; accepted 10 July 2024; published 1 August 2024)

A terahertz radiation enhancing scheme, in which a linearly polarized weakly relativistic laser pulse irradiates a target consisting of two parallel thin-solid layers with a certain gap, is proposed and studied by using two-dimensional particle-in-cell simulations. The radiation is known to be produced by laser-produced hot electrons via mechanisms such as coherent transition radiation at the target surfaces. Under optimized conditions, the energy conversion efficiency of terahertz radiation can be as high as 3.3%, which is nearly 1.5 times higher than that obtained with a single-layer target with the same drive laser. This is mainly due to the enhanced hot electron generation with moderate energy via multiple reflections of the laser pulse between the two target layers. The radiation has two peaks close to  $30^\circ$  from the target surface, which are more collimated than that with the single-layer target. The dependence of the terahertz radiation on a variety of target parameters is given, which can control the terahertz spectrum and radiation efficiency and thus provide guidance for experimental investigations. Moreover, both the coherent transition radiation and antenna radiation models are applied to explain the angular distributions of the terahertz emission found in the simulations.

DOI: [10.1103/PhysRevAccelBeams.27.081301](https://doi.org/10.1103/PhysRevAccelBeams.27.081301)

### I. INTRODUCTION

Terahertz (THz) radiation has many promising applications in broad areas, such as medicine [1], wireless communication [2], security [3], material science [4], environmental remote sensing [5], etc. The generation of THz radiation with high power and efficiency is essential to applications, which remains a critical issue. Recently, THz sources based on laser plasma have attracted widespread attention [6–8]. Unlike those crystal-based THz radiation sources, plasma has a very high damage threshold and thus can suffer very highly intensive laser radiation and thus may drive high power THz sources [9]. Various schemes have been studied on intense laser interaction with solids [10–13], liquids [14], gas targets [15–18], or even electron beams [19–22].

Among the various schemes of laser plasma interactions, the THz radiation efficiency and peak intensity generated by laser solid interaction are particularly prominent. One can generate THz radiation with peak power up to the TW

level [23], far higher than that with a gas target. This is mainly attributed to the high density of solid targets, which allows efficient laser energy coupling with the target, resulting in the generation of more hot electrons and subsequent THz radiation via coherent transition radiation (CTR) or sheath radiation. The CTR from the interaction with laser and solid target has been well studied [24]. Physically, when an ultrashort intense laser pulse interacts with a solid target, the laser ponderomotive force will accelerate target electrons in the solid. When the hot electron bunches transport outside the solid target, THz radiation is produced via CTR [25–27]. The intensity of CTR is related to the number and the energy of charged particles. The more the accelerated electrons, the stronger the radiation energy. The higher the energy of accelerated electrons, the larger the radiation yield. Therefore, many related studies have focused on how to generate more hot electrons or how to enhance the energy of hot electrons.

In addition to the laser interaction with planar solid targets, some other target structures have been proposed, for example, a thin solid target with nanostructures added to the front surface of the target [28,29] and plasma microchannels [30]. Wire targets were also proposed [31–34], which were supposed to be able to guide the hot electron propagation and amplify the THz emission via different mechanisms, such as antenna radiation [35].

\*Contact author: [zmsheng@sjtu.edu.cn](mailto:zmsheng@sjtu.edu.cn)

Published by the American Physical Society under the terms of the [Creative Commons Attribution 4.0 International license](https://creativecommons.org/licenses/by/4.0/). Further distribution of this work must maintain attribution to the author(s) and the published article's title, journal citation, and DOI.

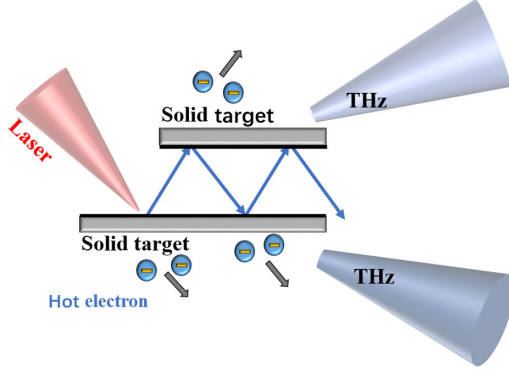


FIG. 1. The configuration of laser interaction with a target composed of two thin layers for THz generation.

In this paper, we propose a new target structure composed of two thin-solid layers for THz generation. As shown schematically in Fig. 1, the laser beam can be reflected multiple times between the two solid layers to achieve higher energy absorption and a larger number of hot electrons as compared to the laser interaction with a single-layer target, thus the efficiency of THz radiation is enhanced.

The paper is organized as follows: In Sec. II, we present simulation results for a typical case of the two-layer target, which are compared with the single-layer case. The physical mechanisms responsible for enhanced THz radiation are analyzed in Sec. III. In Sec. IV, the dependence of THz radiation on the laser and target parameters is given. A summary is given in Sec. V.

## II. SIMULATION RESULTS

We have carried out a two-dimensional simulation with the particle-in-cell (PIC) code epoch [36]. The simulation region is of  $600 \mu\text{m} \times 600 \mu\text{m}$  with  $12000 \times 12000$  grids. The two-layer solid plasma targets, each with a thickness of  $8 \mu\text{m}$ , is separated by a distance of  $50 \mu\text{m}$ . The two target layers have different lengths with  $120 \mu\text{m}$  for the upper one and  $90 \mu\text{m}$  for the lower one. They are tilted by a  $60^\circ$  angle against the  $x$  axis in the simulation box as shown in Fig. 2(a). The length of the second layer of the two-layer target is slightly shorter than that of the first layer so that the laser can be injected relatively easily. To model the preplasma formation in the inner surface between the two target layers, an exponential plasma density profile is assumed with  $n(h) = n_0 \exp(-h/L)$  from  $n_0$  to  $10n_c$ , where  $L = 0.5 \mu\text{m}$  is the scale length,  $n_0 = 0.1n_c$ , and  $n_c = m\omega_0^2/4\pi e^2$  is the critical density of the laser frequency  $\omega_0$ . Here, all the ion particles are immobile and can be seen as the background. For comparison, a single-layer target is also used in the simulation as shown in Fig. 2(b).

A p-polarized laser is incident from the left boundary of the simulation box, propagating along the positive  $x$ -axis direction and injected at the position  $y_0 = -35 \mu\text{m}$ . Therefore, the laser is obliquely incident at  $\theta_i = 30^\circ$  onto the target surface and is reflected between the two layers of

the target. The peak intensity of the laser pulse was  $I_0 = 3.4 \times 10^{17} \text{ W/cm}^2$ , corresponding to the normalized vector potential  $a_0 = eE_0/m_e c \omega_0 = 0.4$  for the laser wavelength  $\lambda_0 = 0.8 \mu\text{m}$ . The laser has Gaussian profiles both along the longitudinal and transverse directions  $a(t) = a_0 \exp(-t^2/T_L^2 - r^2/w_b^2)$  with the full laser duration  $T_L = 5 T_0$ , which is about  $2T_L \ln(2) = 18 \text{ fs}$  in full width at half maximum (FWHM) for the given laser wavelength, where  $T_0 = \lambda_0/c$  is the laser oscillation period. It has a waist size  $w_b = 12.7 \mu\text{m}$ . In the simulation, the laser pulse has the additional phase related to the focus position  $\phi = (2\pi/\lambda_0)(y - y_0)^2/2R_c - \phi_g$ , where  $R_c = x_s[1 + (x_R/x_s)^2]$ ,  $x_R = \pi\omega_0^2/\lambda_0$ ,  $x_s = 310 \mu\text{m}$  so that this laser pulse is focused at  $x = 10 \mu\text{m}$ , which is just around the surface of the first layer target, forming a waist size of  $w_b = 8 \mu\text{m}$  and with a peak amplitude around  $a_0 = 0.64$ . Moreover, both the fields and particles take the open boundaries in the  $x$  and  $y$  directions.

In the following, we show the features of THz emission found with the two-layer target. Figures 2(c) and 2(d) show the spatial distributions of the magnetic field component of produced THz radiation, which are supposed to be produced via the CTR mechanism as studied before [25,26]. It is worth mentioning that we have filtered out the laser (high frequency above 100 THz) in Figs. 2(c) and 2(d), leaving only low frequency THz radiation fields.

In the case of the single-layer target, as we can see in Fig. 2(d), the THz radiation can be divided into two parts, the large circle pulse (as marked with the letter A) and the small circle pulse (as marked with the letter B). The part A is mainly produced by the first interaction between the laser pulse and the target, radiating outward from this point, which has been well studied [26]. While part B comes from the bottom end of the target [33]. Although they are both produced by CTR, they are different in time and space.

In the case of the two-layer target, as we can see in Fig. 2(c), the situation is more complicated. Due to the multiple reflections of the laser pulse between the two solid layers, multiple THz pulses are produced from both the target surfaces (marked as letter C) and both the ends of the targets (marked as letter D). Each interaction can produce transition radiation with a similar pattern to the radiation in Fig. 2(d) and has a similar half-cycle distribution pattern, which is consistent with previous work [25,26]. With the messy superposition of these THz pulses, the spatial distribution of radiation becomes intricate. Figures 2(e) and 2(f) show the angular distributions of the THz radiation spectrum generated by the two-layer target and single-layer target, respectively. Both show broad spectra extending to above 20 THz. The definition of the angle is shown in Fig. 2(a), where we set the propagation direction of the laser beam to be  $\theta = 0^\circ$  and the direction of the target surface to be  $\theta = 60^\circ$ . It is found that the radiation energy is mainly concentrated about  $30^\circ$  and  $90^\circ$ , which are about  $30^\circ$  deviation from the target surface. One can also find that the

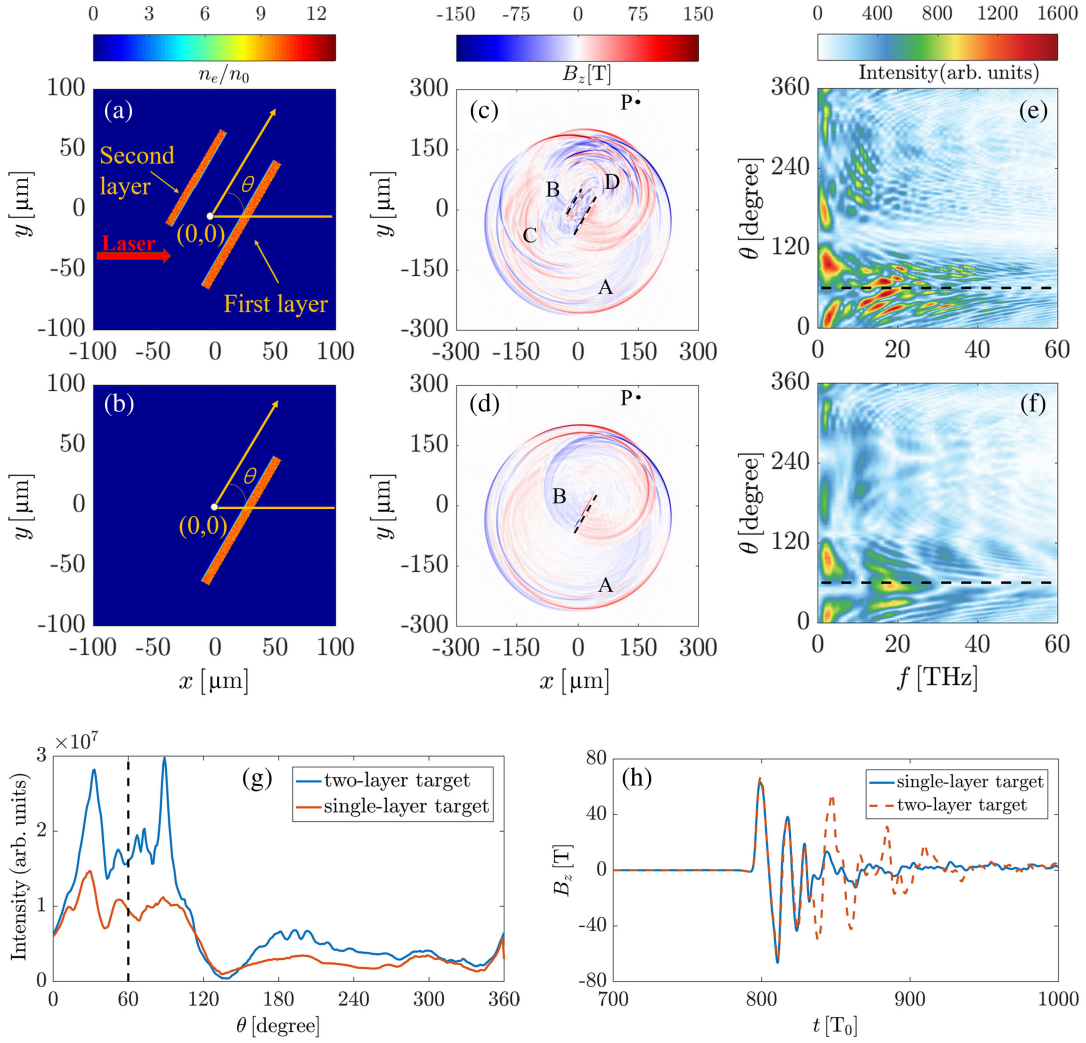


FIG. 2. (a) and (b) are two-dimensional spatial distributions of the target electron density for the two-layer target and single-layer target, respectively; (c) and (d) show snapshots of the magnetic field distributions for the single-layer target and two-layer target, respectively, at  $t = 690 T_0$ , where the black dash lines mark the target positions, the black capital letters (A, B, C, D) mark the different radiation pattern and the point P marks the position  $(x, y) = (150, 150\sqrt{3}) \mu\text{m}$  as a probe point. (e) and (f) show the angular distributions of the radiation frequency spectra for the two cases, respectively, where the black dashed lines indicate the direction of the target surface; (g) The angular distributions of the radiation energy, where the dashed line indicates the target surface direction  $\theta = 60^\circ$ ; (h) The temporal structure of the magnet field (filtered, only keeping the lower frequency) at probe P.

two-layer target model has led to enhanced THz radiation energy as compared to the single-layer target. It is shown that THz radiation is mainly distributed within the angle range from  $20^\circ$  to  $100^\circ$ . The two radiation peaks at  $30^\circ$  and  $90^\circ$  mean that the two-layer targets have a significant enhancement effect on the radiation energy distribution in these directions. This can also be verified in Fig. 2(g), where we compare the angular distributions of integrated THz energy for both cases. In Fig. 2(g), we have integrated the radiation field intensity  $|B_{z-\text{THz}}|^2$ , which only contains the low frequency part (from 0 to 20 THz) in each direction for both cases.

In Fig. 2(h), we compare the temporal profiles of the magnetic field components associated with the THz

radiation (from 0 to 20 THz) produced at the probing point P at  $(x, y) = (150, 150\sqrt{3}) \mu\text{m}$  in the simulation box for both two models. The fields in the first three oscillations look exactly the same because they all come from the interaction with the first layer target, while the consequent radiation fields are associated with subsequent laser interaction with the target and hot electron transport around the target. In the case of the two-layer target, the additional radiation is generated by the second-layer target as shown in Fig. 2(h). It shows that the THz radiation pulse generated by the two-layer target has a significant enhancement.

We have calculated the laser THz energy conversion efficiency. The formula used to calculate the energy conversion efficiency is given by

$$\eta = \frac{\iint |B_{z-\text{THz}}|^2 dx dy}{\iint |B_{z-\text{laser}}|^2 dx dy}, \quad (1)$$

where  $B_{z-\text{THz}}$  and  $B_{z-\text{laser}}$  are the magnetic fields along the  $z$  direction as both the incident laser and THz radiation are  $p$  polarized. When doing this calculation, we use the frequency filtering method to calculate the energy in the THz pulse within 20 THz [37]. For the case with the single-layer target, the conversion efficiency is 2.26%. While for the two-layer target, it has been increased to 3.30%, implying an enhancement of nearly 46% over the single-layer target.

### III. PHYSICAL MECHANISMS FOR THE ENHANCEMENT OF THZ EMISSION

#### A. Comparison of hot electron generation for the two targets

The previous section has shown that the two-layer target can considerably enhance the efficiency of THz generation. To understand the mechanisms, we compare the hot electron generation for the two cases. First, we compare the energy distributions of electrons found from the two types of targets in Fig. 3(a). The inset in the right top corner of Fig. 3(a) shows the electron energy distribution spectra emitted from both the single-layer target and the two-layer target. As shown in this figure,

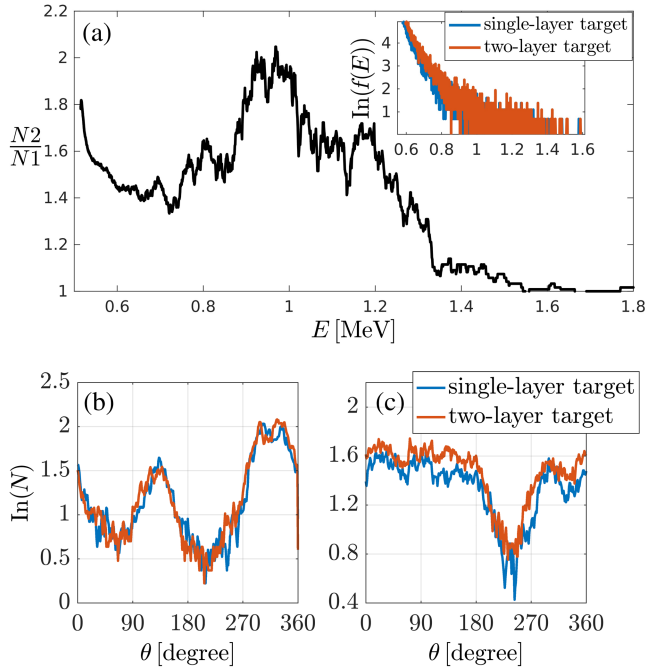


FIG. 3. (a) shows the energy spectra of the hot electrons from both the single-layer target and the two-layer target. while the black line shows the ratio of the two different energy spectra  $\frac{N_2}{N_1} = \frac{N_{\text{two layer}}}{N_{\text{single layer}}}$  at  $t = 690 T_0$ ; (b) and (c) show the angular distributions of the total hot electron number for the two-layer target and single-layer target at time  $t = 412 T_0$  and  $t = 625 T_0$ , respectively.

both the number of hot electrons have the same maximum energy at about 1.5 MeV. These high energy electrons mainly come from the first laser interaction, because the laser has the highest intensity and the minimum focal spot at that time. After the first interaction between the laser and the layer target, the shape of the laser pulse changes, inducing rapid defocusing and its peak intensity decreasing. The black line in Fig. 3(a) shows the ratio of the two different energy spectra  $\frac{N_2}{N_1} = \frac{N_{\text{two layer}}}{N_{\text{single layer}}} \gamma > 1.05$  to further compare these two spectra clearly. It shows that the number of hot electrons produced with the two-layer target is obviously higher than that with the single-layer target, in particular, for hot electrons with energy around 1 MeV. This suggests that the interaction of the reflected pulse with the second layer of the two-layer target can contribute to the generation of considerable hot electrons at a moderate energy level. Therefore, it is clear that the radiation enhancement generated by the two-layer target as compared with the single-layer target is mainly due to the second-layer target. If summing up the number of hot electrons with energy for these two cases, one can find that the two-layer target can produce 43% more hot electrons than the single-layer target. This is consistent with the enhancement of the THz radiation energy conversion rate mentioned above.

The angular distributions of hot electrons with  $\gamma > 1.05$  at  $t = 412 T_0$  and  $625 T_0$  are shown in Figs. 3(b) and 3(c), respectively. It shows that at the early stage when the laser interacts with the first layer of the target, there are two peaks of electron emission near  $-30^\circ$  and  $150^\circ$  as shown in Fig. 3(b), which are close to the target normal at  $-30^\circ$  and  $150^\circ$ . This is in agreement with the theory of electron emission from laser solid interactions [38,39]. At later time, due to the hot electron transport around the target, the electrons are almost uniformly distributed in different directions except for a dip around  $240^\circ$ , i.e., the opposite direction of the target surface.

#### B. Comparison with theory models on angular distributions of THz radiation

To further understand the mechanisms of THz radiation, we will estimate the angular distributions of THz radiation according to the hot electron angular directions given above and the two radiation models, i.e., the CTR model and the antenna model.

At an early stage, the hot electrons are first accelerated by the laser ponderomotive force mediated by the induced electrostatic fields at the solid surface. They are ejected from the target close to the target normal as shown in Fig. 3(b). They can produce THz radiation via the CTR process as schematically shown in Fig. 4(a). The corresponding frequency spectrum and angular distribution can be described by [24–27]

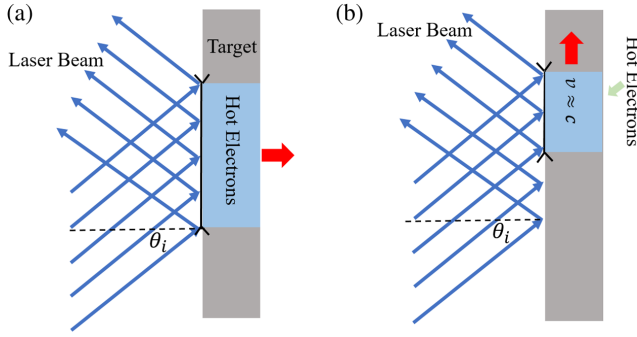


FIG. 4. Two radiation mechanisms associated with the hot electron acceleration and transport process. (a) Coherent transition radiation appears when accelerated hot electrons propagate through the target surface at the beginning; (b) antenna radiation is produced when hot electrons transport along the target surface at a later stage.

$$\frac{d^2\xi_c}{d\omega d\Omega} = \frac{e^2 N(N-1)}{\pi^2 c} \times \left| \int dt dr d\nu S(\beta, \varphi, \theta - \theta_0) f(t, \mathbf{r}, \nu) e^{i\omega t - i\mathbf{k}\cdot\mathbf{r}} \right|^2, \quad (2)$$

where  $\beta$  is the electron velocity normalized by light speed  $c$ ,  $\varphi$  the particle injection direction relative to the target normal,  $\theta$  the observation direction,  $\omega$  the frequency of the radiation, and  $\theta_0$  the target normal direction. While  $f(t, \mathbf{r}, \nu)$  is the electron distribution function related to time  $t$ , space  $\mathbf{r}$ , and velocity  $\nu$ , and  $S$  is given by

$$S(\beta, \varphi, \theta - \theta_0) = \frac{\beta \cos \varphi [\sin(\theta - \theta_0) - \beta \sin \varphi]}{[1 - \beta \sin(\theta - \theta_0) \sin \varphi]^2 - [\beta \cos(\theta - \theta_0) \cos \varphi]^2}. \quad (3)$$

For the given laser parameters in Sec. II, let us estimate the THz radiation angular distribution in the following with the interaction configuration shown in Fig. 4(a). The radiation process takes place in a timescale around  $2T_L + 2w_b \tan(\theta_i)/c$ , and the interaction region has a width of  $2w_b/\cos(\theta_i)$ . Since the laser has a Gaussian distribution both in time and space, the length and the width of the hot electron beam can be estimated to be  $L = 2cT_L + 2w_b \tan(\theta_i)$  and  $r_b = w_b/\cos(\theta_i)$ , respectively. Therefore, the electron beam distribution function can be described with  $f(\mathbf{r}) = (\pi L r_b)^{-1} \exp(-z^2/2L^2 - r^2/2r_b^2)$ , where the longitudinal  $z$  axis is along the target normal direction and it is assumed that the beam electrons have the same velocity  $v\hat{z}$ .

From Eqs. (2) and (3), the radiation spectrum distribution can be estimated with

$$\frac{d^2\xi_c}{d\omega d\Omega} = \frac{e^2 N(N-1)}{\pi^2 c} |S(\beta, \varphi, \theta - \theta_0)|^2 \times \left| \int d\mathbf{r} f(t, \mathbf{r}, \nu) e^{i\omega t - i\mathbf{k}\cdot\mathbf{r}} \right|^2, \quad (4)$$

where

$$\left| \int d\mathbf{r} f(\mathbf{r}) e^{-i\mathbf{k}\cdot\mathbf{r}} \right|^2 = \exp \left[ -\left( \frac{\omega L}{2c} \right)^2 \cos^2(\theta - \theta_0) - \left( \frac{\omega r_b}{c} \right)^2 \sin^2(\theta - \theta_0) \right], \quad (5)$$

The energy angular distribution of this CTR process can be calculated with Eqs. (4) and (5). Here we simply assume that most hot electrons have the relativistic factor  $\gamma = 1.8$ , which is related to the energy peak in Fig. 3(a), corresponding to velocity  $v = 0.832c$ . Due to the fact that the electron beam mainly moves along the target normal, the incident angle  $\varphi = 0$ , laser incident angle  $\theta_i = 30^\circ$ , and target normal direction  $\theta_0 = -30^\circ$  or  $150^\circ$ . For the first laser interaction, the position of the action point is approximately at  $x = -10 \mu\text{m}$ , where the laser waist radius  $w_b$  is around  $8 \mu\text{m}$ . By using Eq. (5), its angular radiation peak is around  $\theta \approx 105^\circ$  or  $15^\circ$  for the radiation frequency  $\omega = 5 \text{ THz}$ , which is around  $45^\circ$  deviation from the target surface, as shown in Fig. 5(a). This radiation is described by the outer circular pattern of the THz fields shown in Figs. 2(c) and 2(d) as marked with letter A.

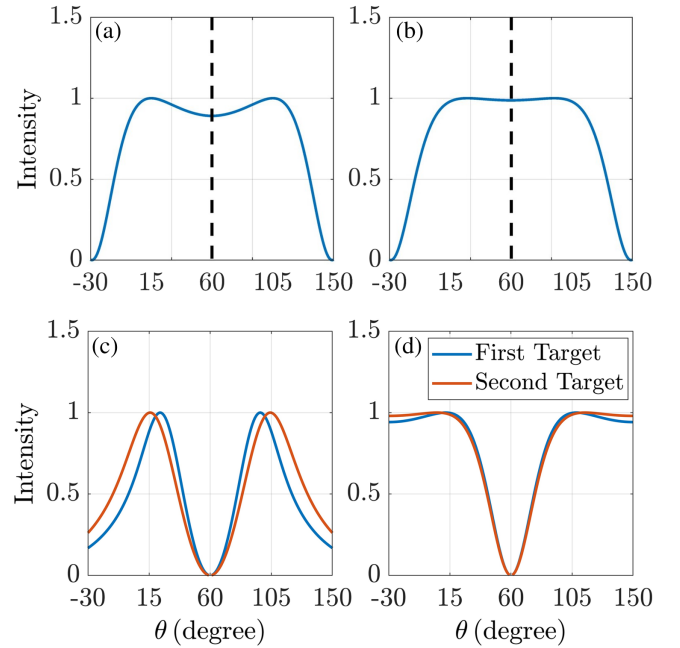


FIG. 5. The normalized angular distribution of the THz radiation from CTR driven by laser target interaction from (a) the first target, (b) the second target, where the black dash lines mark the target positions  $60^\circ$  and the shadow areas represent the energy that will be diffracted to other direction, (c) The normalized angular distributions of the THz emission with antenna model for both two targets with different length. (d) The normalized angular distribution of the THz radiation from the CTR takes place at the end of both targets. All the energy angular distributions are normalized to their own maximum value.

For the laser interaction with the second target, the laser suffered a rapid defocusing and thus its waist radius became  $w_b \approx 11 \mu\text{m}$  at the interaction position. At this time  $2w_b/\cos(30^\circ) > 2cT_L/\cos(60^\circ)$ , so the radius of the electron beam becomes  $r_b = cT_L/\cos(60^\circ)$  the projection of the laser duration on the target surface. From Eq. (5), its angular radiation peak is around  $\theta \approx 27^\circ$  or  $93^\circ$ , which is around  $33^\circ$  deviation from the target surface, as shown in Fig. 5(b). This radiation is responsible for the circular pattern of the THz fields shown in Fig. 2(c) as marked with the letter C. Therefore, the two energy peaks in our PIC simulation shown in Fig. 2(g) are mainly coming from the CTR process from the second target.

As we can see in the Figs. 2(a) and 2(b), a large part of the radiation energy is traveling along the target surface. These radiation fields are superposed at the angle  $\theta \approx 60^\circ$  with phase difference  $\Delta T = D/c$  and  $\Delta T = H/c$ , which is also the main cause for the harmoniclike structure at  $\theta \approx 60^\circ$  in the frequency spectrum as shown in Figs. 2(e) and 2(f). However, when this radiation is emitted from the target end, it will diffract due to the finite target thickness, resulting in the redistribution of the radiated energy. This is only for the radiation, which propagates along the target direction around  $60^\circ$ . As a result, there will be a significant drop in radiation energy around  $60^\circ$ , which also forms the two radiation peaks shown in Fig. 2(g).

However, one can find that the radiation distribution obtained by the above theory is completely symmetrical on both sides of the target normal direction, which does not explain our simulation results. From Fig. 2(g), the radiation energy is clearly concentrated around  $60^\circ$ , rather than  $240^\circ$ , which also indicates that this process may contain a different physical mechanism.

By analyzing the energy spectra of these hot electrons, one can notice there is a valley in the angular direction at  $240^\circ$  in Fig. 3(c), the opposite direction of the target, which means that the majority part of the hot electrons is traveling toward the upper left inside the target. This can be seen as an antenna, and these electrons moving inside this long wirelike target can be considered as a moving current with  $I_s = I_0 \exp(-t^2/2\tau_0^2)(t - z'/c)$ , thus leading to another type of radiation [33] different from the CTR above. This radiation can be described by the Smith model [35],

$$\frac{d^2W}{d\Omega d\omega} = \frac{\mu_0 c I_0^2 \tau_0^2 \sin^2(\theta - \theta_1)}{4\pi[1 - \cos(\theta - \theta_1)]^2} \sin^2 \frac{\omega\tau_d}{2} e^{-\tau_0^2 \omega^2}, \quad (6)$$

where  $\theta$  is still the observation direction, with  $\theta_1 = 60^\circ$  the current moving direction, and  $\tau_d = K/c[1 - \cos(\theta - \theta_1)]$  is the retarded time between the source and the terminal, where  $K$  is the current propagating length. Integrating Eq. (6), we get

$$\frac{dw}{d\Omega} = \frac{\mu_0 c I_0^2 \tau_0^2 \sin^2(\theta - \theta_1)}{16\sqrt{\pi}[1 - \cos(\theta - \theta_1)]^2} (1 - e^{-\tau_d^2/4\tau_0^2}). \quad (7)$$

As shown in Fig. 4(b), during laser interaction, we can assume that some hot electrons are been accelerated along the target direction, and the total accelerated duration is still  $2T_L + 2w_b \tan(30^\circ)/c$ . Assuming that the end point of the electron beam has a velocity  $c$ , the duration  $2\tau_0$  of the electron beam is around  $[2T_L + 2w_b \tan(30^\circ)/c] \times [c/\cos(60^\circ) - c] = [2cT_L + 2w_b \tan(30^\circ)]$ . With  $\tau_0 = T_L + w_b \tan(30^\circ)$  and  $K \approx [120 - (65 - y_0)/\cos(30^\circ)] \mu\text{m} + \tau_0 c \approx 100 \mu\text{m}$  for the first target and  $K \approx [100 - 50/\cot(30^\circ)] \mu\text{m} + \tau_0 c \approx 80 \mu\text{m}$  for the second target, one finds that these radiation peaks appear at  $\theta \approx 60^\circ \pm 37^\circ$  and  $\theta \approx 60^\circ \pm 44^\circ$ , respectively, as shown in Fig. 5(c). Therefore, it is both the interaction of the antenna model and the CTR that will make the radiation much stronger in the direction of  $60^\circ$  than that in the direction of  $240^\circ$ .

In the end, the hot electrons finally eject from the left bottom side of the target and cause another CTR process. We can still use Eq. (2) to describe it. However, at this time, the radius of the electron beam is decided by the thickness of the target, with  $r_b = D/2$  for a uniform transverse distribution and  $l = 2T_L c + 2w_b \tan(30^\circ)$  for a longitudinal Gaussian distribution  $f(z) = 1/(2\pi l)e^{-(z^2/2l^2)}$ . We now have

$$\left| \int dr f(r, \nu) e^{-ik \cdot r} \right|^2 = \exp \left[ -\left( \frac{\omega l}{2c} \right)^2 \cos^2(\theta - \theta_1) \right] \times \left[ \frac{\sin(\omega r_b \cos(\theta - \theta_1)/c)}{\omega r_b \cos(\theta - \theta_1)/c} \right]^2. \quad (8)$$

By using the parameters above, its radiation peaks appear at  $\theta \approx 60^\circ \pm 40^\circ$ , as shown in Fig. 5(d). This radiation is related to the intercircular pattern of the THz fields shown in Figs. 2(c) and 2(d) as marked with letters B and D, respectively. So far, we have explained all the radiation observed in the simulation.

## IV. DEPENDENCE OF THZ RADIATION ON LASER AND TARGET PARAMETERS

### A. Effects of the preplasma

In order to examine the impact of various target and laser parameters on THz emission, we have carried out a series of simulations by varying the preplasma scale  $L$  at the target surface, the distance  $H$  between the two layers of the target, and the laser parameters.

In Fig. 6(a), we compare the conversion efficiency from laser energy to THz radiation under different preplasma scales while keeping all other simulation parameters fixed for the two-layer target and single-layer target. For both cases, it is found that the optimal preplasma scale is around  $0.5 \mu\text{m}$  which is also consistent with the resonance absorption relationship [40]  $L = (c/\omega)[1.47 \sin(30^\circ)]^{-3}$ .

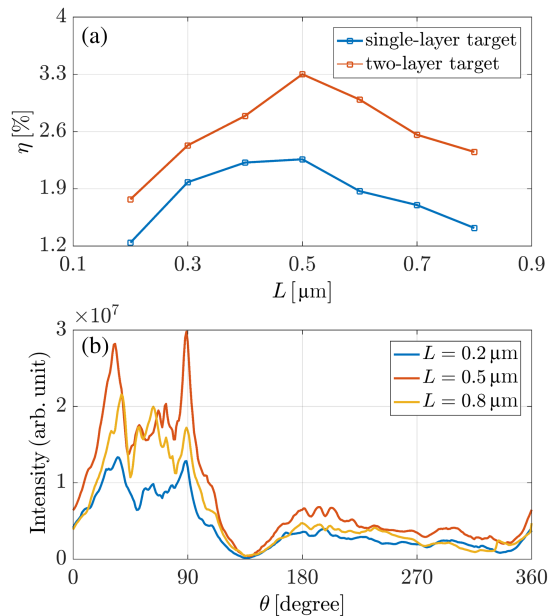


FIG. 6. (a) The conversion efficiency from laser energy to THz energy for different preplasma lengths, where the red line is found for the two-layer target and the blue line is for the single-layer target. (b) The angular distributions of the THz emission with different preplasma lengths found for the two-layer target.

At this time, both the two-layer target model and single-layer model reach their maximum conversion efficiency rate, corresponding to the conversion efficiency of 3.30% and 2.26%, respectively.

In Fig. 6(b), we show the energy angular distribution of THz radiation corresponding to different preplasma scales for the two-layer target. When the preplasma scale is well situated, the radiation is sharply peaked at  $30^\circ$  and  $90^\circ$ . As we know, the preplasma scale length plays a significant role in THz radiation. The optimal scale length of preplasma occurs mainly due to the fact that the number of produced hot electrons, rather than their average energy, is the largest.

### B. Effects of the gap distance between the two thin layers

Now we focus on the two-layer target and study the effect of the layer gap on THz emission. In Fig. 7(a), the THz emission conversion efficiency is shown as a function of the gap distance between the two layers while keeping all other simulation parameters fixed. It is shown that the optimal distance is around  $50 \mu\text{m}$ , corresponding to a conversion efficiency of 3.30%. In Fig. 7(b), we show the angular distributions of THz emission for different gap distances.

Now let us briefly analyze the effect of gap distances on radiation distribution. For the whole process, in fact, the target gap distance affects the position of the interaction and the defocus of the laser beam.

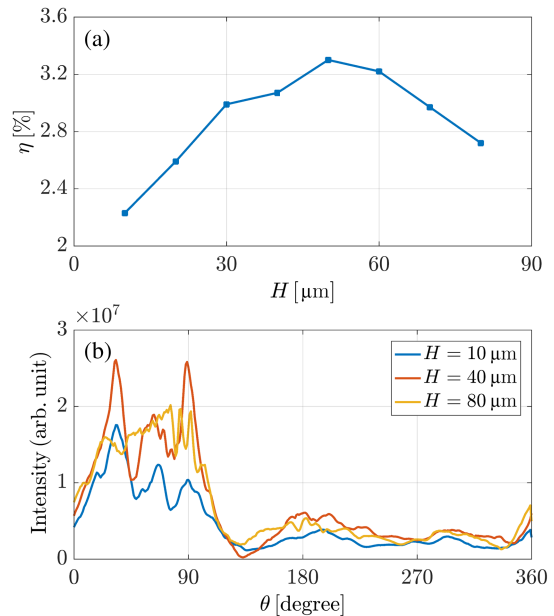


FIG. 7. (a) The conversion efficiency from laser energy to THz energy with different gap distances between two layers. (b) The angular distributions of the THz emission with different gap distances.

When the distance between the two targets is too narrow, part of the THz radiation generated by multiple reflections will be trapped between the two targets and reflected back and forth and will finally be absorbed by the preplasma at the surface of the target. A narrow gap will also prevent the laser pulse from propagating between the two targets as the entrance will block part of the incident laser energy and thus cause energy loss. When the distance gap is too wide, the laser interaction with the second target will be significantly reduced due to the rapid defocusing of the laser beam. The larger the target gap distance, the larger the laser focal spot radius when the laser interacts with the target. An excessive gap distance will cause only a portion of the laser to act on the target surface, resulting in efficiency loss.

By using Eq. (5), a laser with a large width  $w_b$  will generate a longer hot electron beam  $l = 2cT_L + 2w_b \tan(30^\circ)$  and thus move the peak of the radiation distribution away from the target direction  $60^\circ$ . When the hot electron beam grows to a certain length, the radiation along the target direction will dominate, exceeding the two peaks on the other angle, making the radiation energy more concentrated in the target direction as shown in Fig. 7(b). Therefore, changing the gap distance can be a method to manipulate the radiation spatial distribution in our model. It will be easy to adjust the gap distance between the two-layer targets in experiments in order to obtain the corresponding radiation pattern, either enhancing or reducing the directionality of the THz radiation. In the present simulation, it is found that when the gap distance is about  $50 \mu\text{m}$ , there are well-defined radiation peaks at about  $30^\circ$  and  $90^\circ$ . However, the gap distance does not have a great impact on the frequency of the radiation as it

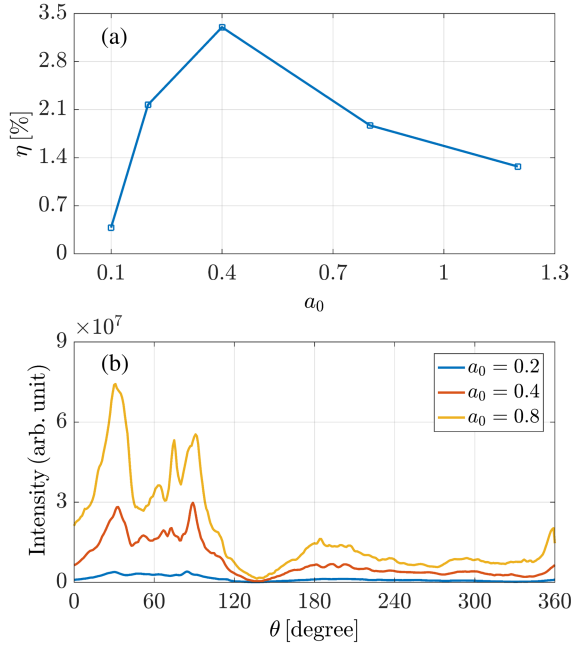


FIG. 8. (a) The conversion efficiency from laser energy to THz energy with different parameters of laser intensity. (b) The angular distributions of the THz emission with different laser peak amplitudes.

just controls the delay between those pulses in the time domain.

### C. Effects of the laser pulse intensity and the incident angle

In this subsection, we focus on the effect of the laser pulse intensity and the incident angle  $\theta_i$  on THz emission. In Fig. 6, we change the laser intensity while keeping all the other simulation parameters unchanged and display the simulation result. As we can see in Fig. 8(a), there is an optimal intensity for the laser pulse if just considering the conversion efficiency. It is shown that the optimal intensity is around  $a_0 = 0.4$ , corresponding to the conversion efficiency of 3.30%.

In Fig. 8(b), we show the angular distributions of THz emission for different laser intensities. However, despite the strength of the THz radiation, the distribution of the THz is similar and has the same peak position. The laser intensity just alters the intensity of the THz radiation.

In Fig. 9, we show the angular distributions of THz emission for different  $\theta_i$ . In our simulation, we change the angle of the two-layer target while keeping the laser parameter unchanged so as to change the  $\theta_i$ . As the incident angle decreased, the THz energy rapidly dropped, while the distributions of the THz became more concentrated, the same as the work in [26], which can also match with Eq. (4).

However, we do not demonstrate the  $\theta_i$  larger than  $60^\circ$  or smaller than  $30^\circ$ . For  $\theta_i$  smaller than  $30^\circ$ , it will be hard for

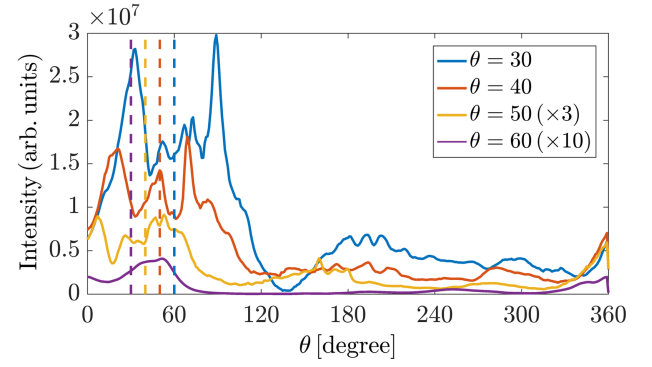


FIG. 9. The angular distributions of the THz emission with different laser incident angle  $\theta_i$  while the dash lines are the direction of the target corresponding to the angular distributions with the same color.

the laser beam to enter the middle region between the two-layer target, while a much larger  $\theta_i$  will increase the time it takes for the laser to reflect from the first target to the second target  $H/\cos(\theta_i)c$ . This also exacerbates the defocusing process of the laser and causes only a portion of the laser to act on the target surface, the same negative effect with an excessive gap distance.

The optimal angle can also be calculated by  $\theta_m = \arcsin(0.68(\omega L/c)^{-1/3}) \approx 27^\circ$ , when  $L = 0.5 \mu\text{m}$ , which is consistent with the resonance absorption [40].

### D. Dependence of THz frequency on laser pulse duration and target-layer thickness

In Fig. 10, we change the laser duration while keeping all other simulation parameters unchanged and display the radiation frequency and angular distribution for different

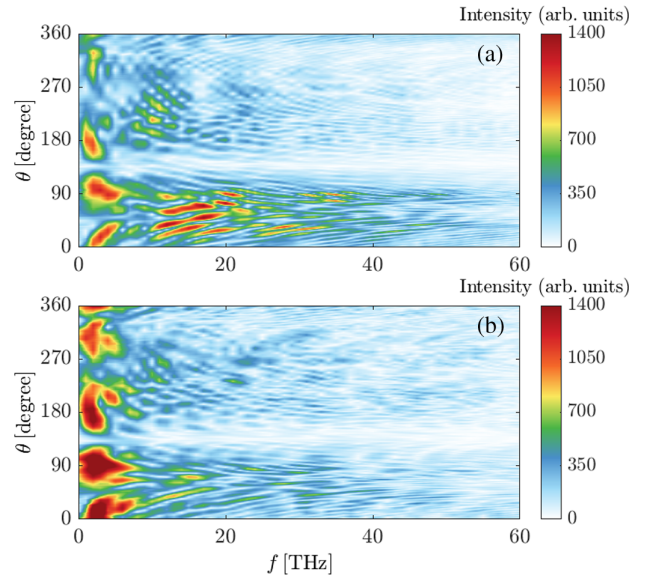


FIG. 10. The angular distributions of the radiation spectra with different laser pulse duration: (a)  $T_L = 4 T_0$ ; (b)  $T_L = 25 T_0$ .

laser durations. When the pulse duration is  $T_L = 4 T_0$ , the radiation spectra become very broad, extending to 30 THz, as shown in Fig. 10(a). As the laser duration increases, the high frequency component of THz radiation disappears, as shown in Fig. 10(b) for pulse duration of  $25 T_0$ . This is mainly because the length of the hot electrons generated by the interaction between the laser and targets is mainly related to the pulse duration. The larger the pulse duration the longer the relevant electron beam, thus resulting in a longer radiation pulse duration. When the width of the radiation pulse is close to the duration of the hot electrons refluxing in the target, which corresponds with the thickness of the target (in this simulation, the duration is around  $30 T_0$ ), the first pulse generated by the interaction will merge with the second pulse, thus resulting in a decrease in radiation frequency.

To get a high conversion efficiency, the laser pulse duration has to be short, while a longer laser pulse contains more energy and can accelerate more electrons, so there is a trade-off here.

When the target thickness is changed, the radiation frequency is also expected to be changed. In Fig. 11, we changed the thickness of the target and displayed the radiation frequency and angular distributions corresponding to the thickness parameters of the target. From this figure, it is not difficult to see that as the thickness of the target increases, the high frequency part of the THz radiation moves toward the lower frequency. The THz frequency is also related to the interval of each THz pulse generated by transition radiation, and the interval of the pulses is determined by the time when the hot electron reflux passes through the target. Therefore, the thicker the target, the longer the time electrons need to travel through

the target and thus the lower the frequency of radiation. Therefore, one finds that the pulse duration of the laser and the thickness of the target are the only two parameters in the model that can control the radiation frequency. However, a thicker target will reduce the energy of the hot electrons that travel through the target [26] and reduce the conversion rate. Thus, a thinner target is still a better choice.

## V. SUMMARY

In this paper, we propose to irradiate an intense laser pulse onto a two-layer target consisting of two parallel thin layers to enhance THz emission efficiency based upon PIC simulations. This not only leads to the improved conversion efficiency of THz radiation but also modifies the angular distribution of the radiation, i.e., the THz radiation becomes more collimated. Its main mechanism is due to the generation of more hot electrons with moderate energy via multiple reflections of the laser pulse between two layers of the target. The physical mechanisms responsible for the THz radiation found in the simulation are discussed. It is suggested that both the coherent transition radiation and antenna radiation are involved, which are also corroborated by the simulation results. Finally, the effects of laser and target parameters on the conversion efficiency, THz spectrum, and angular distributions are investigated numerically, which provide useful reference for future related experiments.

## ACKNOWLEDGMENTS

This work is supported by the National Natural Science Foundation of China (Grants No. 12135009, No. 11991074, No. 11975154, and No. 12005287).

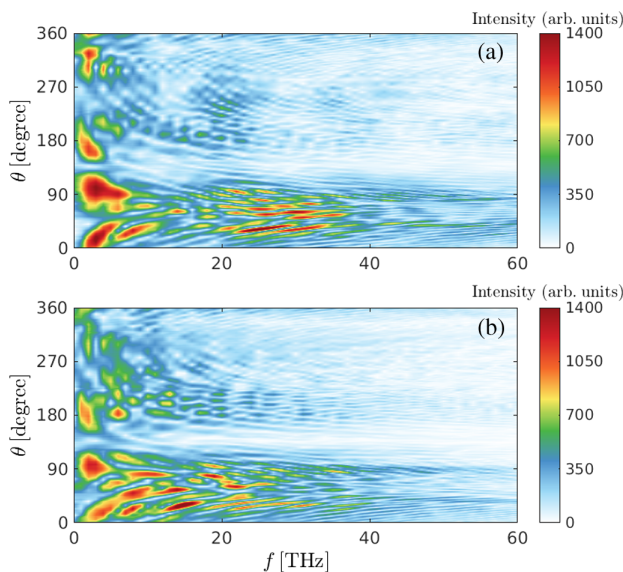


FIG. 11. The angular and frequency distributions of the radiation with different target-layer thickness: (a)  $D = 4 \mu\text{m}$ ; (b)  $D = 16 \mu\text{m}$ .

- [1] J. H. Son, *Terahertz Biomedical Science and Technology* (CRC Press, Boca Raton, 2014), 10.1201/b17060.
- [2] T. Nagatsuma, S. Horiguchi, Y. Minamikata, Y. Yoshimizu, S. Hisatake, S. Kuwano, N. Yoshimoto, J. Terada, and H. Takahashiet, Terahertz wireless communications based on photonics technologies, *Opt. Express* **21**, 23736 (2013).
- [3] M. C. Kemp, P. F. Taday, B. E. Cole, J. A. Cluff, A. J. Fitzgerald, and W. R. Tribe, Security applications of terahertz technology, *Proc. SPIE Int. Soc. Opt. Eng.* **5070**, 44 (2003).
- [4] B. Ferguson and X. C. Zhang, Materials for terahertz science and technology, *Nat. Mater.* **1**, 26 (2002).
- [5] J. Liu, J. Dai, S. L. Chin, and X. C. Zhang, Coherent ballistic motion of electrons in a periodic potential, *Nat. Photonics* **4**, 627 (2010).
- [6] G. P. Williams, Filling the THz gap—high power sources and applications, *Rep. Prog. Phys.* **69**, 301 (2005).
- [7] W. Kuehn, P. Gaal, K. Reimann, M. Woerner, T. Elsaesser, and R. Hey, Coherent ballistic motion of electrons in a periodic potential, *Phys. Rev. Lett.* **104**, 146602 (2010).

- [8] H. G. Roskos, M. D. Thomson, M. Kieß, and A. T. Löffler, Broadband THz emission from gas plasmas induced by femtosecond optical pulses: From fundamentals to applications, *Laser Photonics Rev.* **1**, 349 (2007).
- [9] D. H. Auston, K. P. Cheung, J. A. Valdmanis, and D. A. Kleinman, Cherenkov radiation from femtosecond optical pulses in electro-optic media, *Phys. Rev. Lett.* **53**, 1555 (1984).
- [10] Y. Gao, T. Drake, Z. Chen, and M. F. DeCamp, Half-cycle-pulse terahertz emission from an ultrafast laser plasma in a solid target, *Opt. Lett.* **33**, 2776 (2008).
- [11] Y. T. Li, C. Li, M. L. Zhou, W. M. Wang, F. Du, W. J. Ding, X. X. Lin, F. Liu, Z. M. Sheng, X. Y. Peng *et al.*, Strong terahertz radiation from relativistic laser interaction with solid density plasmas, *Appl. Phys. Lett.* **100**, 254101 (2012).
- [12] G. Q. Liao, Y. T. Li, Y. H. Zhang, H. Liu, X. L. Ge, S. Yang, W. Q. Wei, X. H. Yuan, Y. Q. Deng, B. J. Zhu *et al.*, Demonstration of coherent terahertz transition radiation from relativistic laser-solid interactions, *Phys. Rev. Lett.* **116**, 205003 (2016).
- [13] C. Li, G. Q. Liao, and Y. T. Li, Non-scanning systems for far-infrared radiation detection from laser-induced plasmas, *High Power Laser Sci. Eng.* **3**, 2331 (2015).
- [14] Q. Jin, E. Yiwen, K. Williams, J. Dai, and X. C. Zhang, Observation of broadband terahertz wave generation from liquid water, *Appl. Phys. Lett.* **111**, 071103 (2017).
- [15] M. Chen, A. Pukhov, X. Y. Peng, and O. Willi, Theoretical analysis and simulations of strong terahertz radiation from the interaction of ultrashort laser pulses with gases, *Phys. Rev. E* **78**, 046406 (2008).
- [16] W. M. Wang, P. Gibbon, Z. M. Sheng, and Y. T. Li, Tunable circularly polarized terahertz radiation from magnetized gas plasma, *Phys. Rev. Lett.* **114**, 253901 (2015).
- [17] Z. M. Sheng, K. Mima, J. Zhang, and H. Sanuki, Emission of electromagnetic pulses from laser wakefields through linear mode conversion, *Phys. Rev. Lett.* **94**, 095003 (2005).
- [18] P. Gonzalez de Alaiza Martinez, X. Davoine, A. Debayle, and L. Bergé, Terahertz radiation driven by two-color laser pulses at near-relativistic intensities: Competition between photoionization and wakefield effects, *Sci. Rep.* **6**, 26743 (2016).
- [19] L. Shi, S. L. Johnson, and S. Reiche, Compact and powerful THz source investigation on laser plasma wakefield injector and dielectric lined structure, *Phys. Rev. Accel. Beams* **23**, 014701 (2020).
- [20] Z. Zhang, L. Yan, Y. Du, W. Huang, C. Tang, and Z. Huang, Generation of high-power, tunable terahertz radiation from laser interaction with a relativistic electron beam, *Phys. Rev. Accel. Beams* **20**, 050701 (2017).
- [21] S. Bielawski, C. Evain, T. Hara, M. Hosaka, M. Katoh, S. Kimura, A. Mochihashi, M. Shimada, C. Szwaj, T. Takahashi, and Y. Takashima, Tunable narrowband terahertz emission from mastered laser–electron beam interaction, *Nat. Phys.* **4**, 390 (2008).
- [22] J. M. Byrd, Z. Hao, M. C. Martin, D. S. Robin, F. Sannibale, R. W. Schoenlein, A. A. Zholents, and M. S. Zolotarev, Tailored terahertz pulses from a laser-modulated electron beam, *Phys. Rev. Lett.* **96**, 164801 (2006).
- [23] G. Q. Liao, H. Liu, G. G. Scott, Y. H. Zhang, B. J. Zhu, Z. Zhang, Y. T. Li, C. Armstrong, E. Zemaityte, P. Bradford *et al.*, Towards terawatt-scale spectrally tunable terahertz pulses via relativistic laser-foil interactions, *Phys. Rev. X* **10**, 031062 (2020).
- [24] J. Zheng, K. A. Tanaka, K. A. Tanaka, T. Miyakoshi, Y. Kitagawa, R. Kodama, T. Kurahashi, and T. Yamanaka, Theoretical study of transition radiation from hot electrons generated in the laser–solid interaction, *Phys. Plasmas* **10**, 2994 (2003).
- [25] W. J. Ding, Z. M. Sheng, and W. S. Koh, High-field half-cycle terahertz radiation from relativistic laser interaction with thin solid targets, *Appl. Phys. Lett.* **103**, 204107 (2013).
- [26] W. J. Ding and Z. M. Sheng, Sub GV/cm terahertz radiation from relativistic laser-solid interactions via coherent transition radiation, *Phys. Rev. E* **93**, 063204 (2016).
- [27] C. Settakorn, Generation and use of coherent transition radiation from short electron bunches, Ph.D. thesis, Stanford University, 2001.
- [28] S. Mondal, Q. Wei, W. J. Ding, H. A. Hafez, M. A. Fareed, A. Laramée, X. Ropagnol, G. Zhang, S. Sun, Z. M. Sheng *et al.*, Aligned copper nanorod arrays for highly efficient generation of intense ultra-broadband THz pulses, *Sci. Rep.* **7**, 40058 (2017).
- [29] I. V. Konoplev, All-metal wakefield accelerator: Two-dimensional periodic surface lattices for charged particle acceleration. *Phys. Rev. Accel. Beams* **25**, 111302 (2022).
- [30] L. Yi and T. Fülöp, Coherent diffraction radiation of relativistic terahertz pulses from a laser-driven microplasma waveguide, *Phys. Rev. Lett.* **123**, 094801 (2019).
- [31] D. Zhang, Y. Zeng, Y. Bai, Z. Li, Y. Tian, and R. Li, Coherent surface plasmon polariton amplification via free-electron pumping, *Nature (London)* **611**, 55 (2022).
- [32] R. Kodama, Y. Sentoku, Z. L. Chen, G. R. Kumar, S. P. Hatchett, Y. Toyama, T. E. Cowan, R. R. Freeman, J. Fuchs, Y. Izawa *et al.*, Plasma devices to guide and collimate a high density of MeV electrons, *Nature (London)* **432**, 1005 (2004).
- [33] H. B. Zhuo, S. J. Zhang, X. H. Li *et al.*, Terahertz generation from laser-driven ultrafast current propagation along a wire target, *Phys. Rev. E* **95**, 013201 (2017).
- [34] N. Bukharskii and Ph. Korneev, Intense widely controlled terahertz radiation from laser-driven wires, *Matter Radiat. Extremes* **8**, 044401 (2023).
- [35] G. S. Smith and T. W. Hertel, On the transient radiation of energy from simple current distributions and linear antennas. *IEEE Antennas Propag. Mag.* **43**, 49 (2001).
- [36] T. D. Arber, K. Bennett, C. S. Brady, A. Lawrence-Douglas, M. G. Ramsay, N. J. Sircombe, P. Gillies, R. G. Evans, H. Schmitz, A. R. Bell, and C. P. Ridgers, Contemporary particle-in-cell approach to laser-plasma modelling, *Plasma Phys. Controlled Fusion* **57**, 113001 (2015).
- [37] C. A. Greene, K. Thirumalai, K. A. Kearney, J. M. Delgado, W. Schwanghart, N. S. Wolfenbarger, K. M. Thyng, D. E. Gwyther, A. S. Gardner, and D. D. Blankenship, The climate data toolbox for MATLAB, *Geochem. Geophys. Geosyst.* **20**, 3774 (2019).

- [38] Z.-M. Sheng, Y. Sentoku, K. Mima, J. Zhang, W. Yu, and J. Meyer-ter-Vehn, Angular distributions of fast electrons, ions, and bremsstrahlung x/ gamma-rays in intense laser interaction with solid targets, *Phys. Rev. Lett.* **85**, 5340 (2000).
- [39] M. Chen, Z.-M. Sheng, and J. Zhang, On the angular distribution of fast electrons generated in intense laser interaction with solid targets, *Phys. Plasmas* **13**, 014504 (2006).
- [40] Y.-Q. Cui, W.-M. Wang, Z.-M. Sheng, Y.-T. Li, and J. Zhang, Laser absorption and hot electron temperature scalings in laser-plasma interactions, *Plasma Phys. Controlled Fusion* **55**, 085008 (2013).